Compressive Spectral Imaging via Polar Coded Aperture

Chen Fu, *Student Member, IEEE, Michael Don, Member, IEEE* and Gonzalo R. Arce, *Fellow, IEEE*

***Abstract*—A compressive spectral imager based on a polar coded aperture and a continuous variable circular bandpass filter is proposed for spinning munitions. As the imager rotates with the munition, compressive projections are sequentially captured with embedded spatial and spectral modulation. The polar coded aperture design is introduced, aiming at optimizing the sensing process. Both discrete and continuous rotation models of the proposed imager are derived and used to characterize the compressive imager. Computer simulations validate the computational models and the reconstruction algorithm.**

***Index Terms*—Compressed sensing, Image coding, Polar coded aperture, Circular viable filter, Continuous rotation model.**

I. Introduction

IMAGING techniques have been introduced in guided munitions to perform precise target detection and pinpoint strike capabilities. They have many advantages over global positioning system (GPS) driven systems, such as jamming immunity and greater accuracy as demonstrated in many unmanned aerial vehicle (UAV) platforms [1-5]. Typically, monochromatic imaging is used in these applications. Spectral imaging, however, is capable of increasing the precision in target detection and munition guidance by providing additional spectral information of the scene [6,7]. Spectral imaging architectures usually involve moving filters [8] or the application of expensive color patterned imaging sensor arrays [9,10] to achieve spectral modulation. The spinning nature of munitions provides an approach to modulate the spectrum via a circular variable filter (CVF) without the need for moving parts. A CVF is a bandpass filter whose center wavelength continuously varies with its angular position and has a history of being used in spectrometers, monochrometers, and spectral imagers [11-18]. When mounted on a spinning munition, the CVF provides a continuous spectral modulation of the target.

In addition to spectral modulation, the munition's spin can also be leveraged to increase the spatial resolution of the imager using compressive sensing (CS) theory. In CS, a compressive sample is normally acquired by applying a binary code in the spatial domain [19-22]. Besides increased resolution, compressive imaging can provide faster measurement acquisition, easy data storage and transmission, as well as reduced system noise. Thus, a new compressive spectral imager is proposed for spinning munitions that combines a CVF with a coded aperture.

Although several coded aperture compressive spectral imagers have been developed recently [19,23-27], our design has three advantages over existing designs. First, in traditional coded aperture compressive imaging, a square shaped coded photomask was initially used to provide spatial coding for a single snapshot. To capture additional snapshots, elaborate mechanisms are typically employed to apply multiple codes, such as using a digital micro-mirror device (DMD) or by shifting an aperture code with a piezoelectric actuator [26-29]. These complex, expensive architectures are not suited to munitions, however, which require a simple, inexpensive imager. Our design solves this problem by using a polar shaped coded mask together with the munition's natural spin to obtain multiple snapshots without any moving parts or complex devices. Secondly, although spatial super-resolution methods have been presented [25], traditional coded aperture compressive spectral imagers usually employ coded apertures the same size as the focal plane array (FPA) sensors, thus limiting the resolution of the spectral image to that of the FPA [19,23-28]. However, this is unnecessary since the reconstructed spatial resolution is only determined by the resolution of the coded aperture. Instead, a low resolution FPA is applied here with less expense on munition applications. Sufficient measurements are captured through the imager rotation with a high-resolution coded aperture. Third, in traditional compressive spectral imagers, one or more dispersive elements are typically applied to produce spectral separation [23,24]. However, the non-linear spectral dispersion makes the spectrum sampling non-uniform. A high-order model is needed to characterize the dispersion, increasing the complexity of modeling and calibration [30]. Our design solves this problem by using a CVF, which has a linear spectral modulation. Combined with the polar coded aperture, the CVF is placed on the focal plane of the objective lens, making our imager more compact than other existing coded aperture compressive spectral imagers.

Challenges exist when developing the coded aperture design. The spatial coding provided by conventional square shaped coded apertures requires complex rotation transformations. Additionally, the coded aperture provides less modulation towards its center, resulting in an inefficient sensing strategy. Different from traditional square coded apertures in compressive imaging [19-30], we propose a polar coded aperture with a spokes-rings structure to solve the above problems. The rotation motion is transformed into a simple circular shifting of image pixels which provides uniform modulation.

Figure 1 shows the proposed imaging architecture which consists of an objective lens, a polar coded aperture, a CVF,

C. Fu and G. R. Arce are with the Department of Electrical and Computer Engineering, University of Delaware, Newark, DE 19716. USA.

Michael Don is a Electrical Engineer with United States Army Research Laboratory, Aberdeen Proving Ground, MD, 21005, USA.

This research was supported in part by the Army Research Office (ARO) under the contract W911NF-12-1-0380, the Defense University Research Instrumentation Program (DURIP) under the contract W911NF-14-1-0522, and B&W Tek, Inc.

This article has been accepted for publication in a future issue of this journal, but has not been fully edited. Content may change prior to final publication. Citation information: DOI 10.1109/TCI.2016.2617740, IEEE Transactions on Computational Imaging

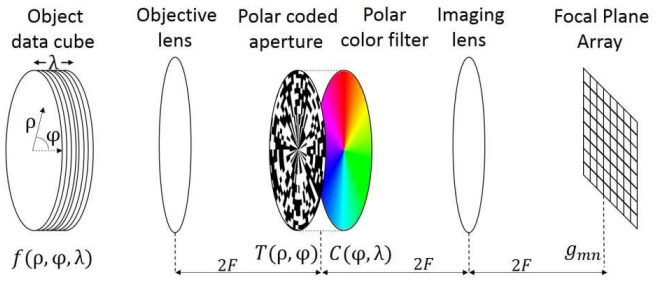

Figure 1. Compressive spectral imaging architecture with a polar coded aperture and a continuous viable circular bandpass filter. Compressed projections are captured on the FPA detector.

a relay lens and a focal plane array (FPA) detector. The polar coded aperture, combined with the continuous circular variable bandpass filter, are placed in the image focal plane of the objective lens, providing the spatial and spectral modulation to the scene. As the munition spins, the imager conducts a continuous rotation. In general, the imager can also be mounted on other spinning equipment, or simply on a electronic controlled rotating platform to perform compressive spectral imaging.

For guided munitions, the motion of the imager can be described in multiple dimensions. The translation motion should be precisely acquired for characterizing the compressive sensing reconstruction. In this paper, only a two-dimensional rotation is considered for simplicity, with the rotation speed assumed to be constant and known a priori. For further research, the robustness of the system should also be evaluated by calculating the tolerance of the rotation modelling error.

The main contributions of this paper are addressed in three aspects: First, a novel method of changing spatial coding for compressive imaging is developed by the rotation of a polar coded aperture. The geometry design of the polar aperture is presented to optimize the image quality. Second, the CVF is introduced into compressive spectral imaging. To our knowledge, this is the first time a CVF is applied to compressive coded aperture imaging. The influence of CVF bandwidth to the reconstruction quality is analysed. Finally, both the discrete and continuous rotation forward models are developed with the corresponding computer simulation results presented.

II. Polar Coded Aperture Compressive Spectral Imaging System

A. Spectral Imaging via Compressive Sensing

Natural scenes typically contain correlations among neighbourhood image points and between adjacent spectral bands [31]. Thus the spectral images can be represented in some basis with a small number of nonzero coefficients. The sparsity of the spectral images enables the application of compressive sensing in the imaging procedure. Denote the vector $\mathbf{f}$ as the collection of the desired spectral image pixels, and denote $\mathbf{g}$ as the vector formed by the CCD measurements. Then the sensing procedure can be expressed as

$$\mathbf{g} = \mathbf{H}\mathbf{f}, \tag{1}$$

where $\mathbf{H}$ is the sensing matrix of the imaging system. With a proper selected basis $\mathbf{\Psi}$, $\mathbf{f}$ can be represented as $\mathbf{f} = \mathbf{\Psi}\boldsymbol{\theta}$, where the coefficients vector $\boldsymbol{\theta}$ is sparse. Thus the sensing procedure is rewritten as

$$\mathbf{g} = \mathbf{H}\mathbf{\Psi}\boldsymbol{\theta} = \mathbf{A}\boldsymbol{\theta}, \tag{2}$$

where $\mathbf{A} = \mathbf{H}\mathbf{\Psi}$. Given the measurements $\mathbf{g}$ with the number of elements much smaller than the desired vector $\mathbf{f}$, the inverse problem can be solved with high accuracy by reconstruction algorithms [19,31]. A good knowledge of the sensing matrix $\mathbf{H}$ is critical to an accurate reconstruction. Thus in this section, a detailed mathematical modelling of the sensing matrix is presented.

B. Discrete Imager Rotation Sensing Model

The proposed compressive imaging architecture is displayed in Figure 1. A polar coded aperture combined with a continuous variable circular bandpass filter is applied at the image focal plane to provide spatial and spectral compressive coding. The polar coded aperture is designed to have a ring-spoke structure as shown in Fig. 2. The aperture consists R_{in} inner rings and R_{out} outer rings. The outer rings are designed to have a denser distribution of spokes than the inner rings. S_{in} and S_{out} are denoted as the numbers of spokes in the inner and outer rings, respectively. The design of the aperture geometry is further introduced in Section III.

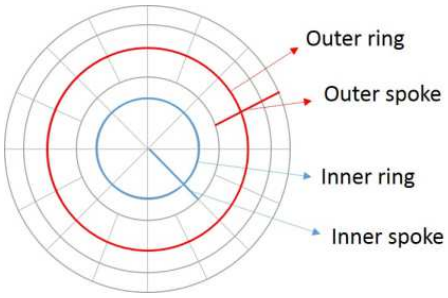

Figure 2. Geometry illustration of the proposed polar coded aperture. The number of spokes in outer rings is twice of the spokes in inner rings.

Compressed FPA projections of the coded data cube are captured as the imager rotates. If the image rotations are generated by electronic devices, the rotation can be controlled to have discrete angle increments, where the imager remains fixed during one snapshot measurement. When the imager is mounted on a spinning munition, continuous rotation motion occurs when measurements are captured. However, if the shutter time τ_s of the camera is much smaller than the rotation period of the imager τ_r, $\tau_s << \tau_r$, the imager can be assumed to be static during each snapshot. With this assumption, a discrete approximation model of the imager rotation is described next. In Section V, a continuous rotation model is further developed.

Denote the scene as a 3D data cube $f(\varphi,\rho,\lambda)$, where φ and ρ are the spatial polar coordinates, and λ is the spectral wavelength. The polar coded aperture is represented as $T(\varphi,\rho)$, while the continuous variable circular bandpass filter is modeled as $C(\varphi,\lambda)$. The center wavelengths of the polar bandpass filter continuously change in the range of

This article has been accepted for publication in a future issue of this journal, but has not been fully edited. Content may change prior to final publication. Citation information: DOI 10.1109/TCI.2016.2617740, IEEE Transactions on Computational Imaging

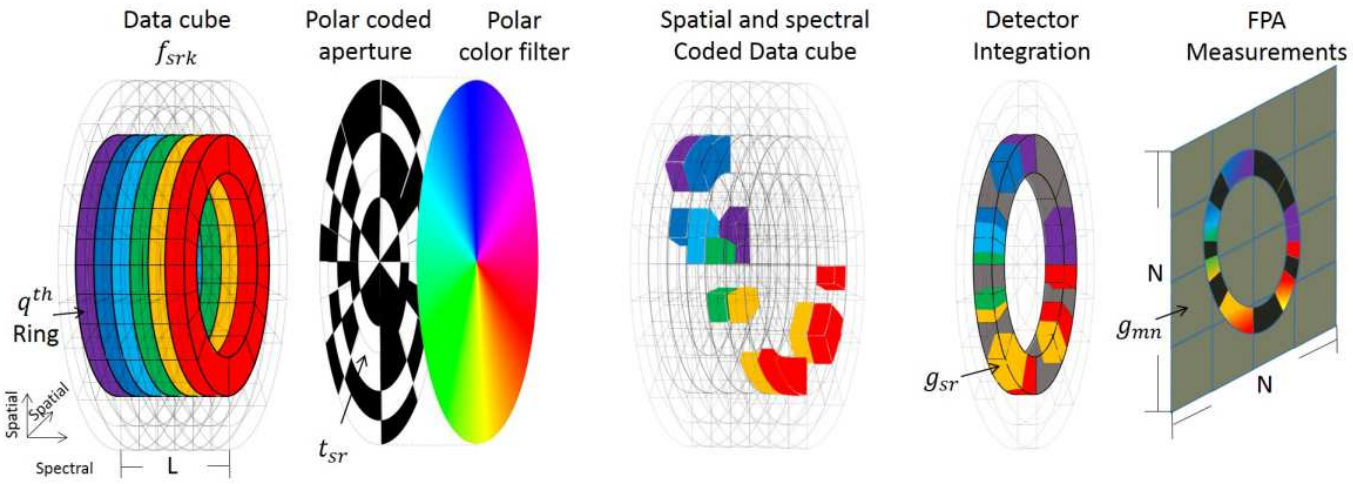

Figure 3. Discretized compressive sensing phenomenon of polar imager. The q^{th} ring of the data cube f_{srk} is coded by the polar coded aperture and modulated by the continuous variable circular bandpass filter. The modulated light is integrated in both spatial and spectral domains, captured by the FPA sensors.

$[\lambda_{min}, \lambda_{max}]$ with φ increasing from 0 to 2π. The bandwidth of the bandpass filter is denoted as b_w for all φ. Thus the transmitted wavelength range of the continuous variable circular bandpass filter is $[\lambda_{min} - b_w/2, \lambda_{max} + b_w/2]$. The polar coordinates representation of the FPA projection is written as:

$$g_p(\varphi, \rho) = T(\varphi, \rho) \int_{\lambda_{min}-b_w/2}^{\lambda_{max}+b_w/2} C(\varphi, \lambda) f(\varphi, \rho, \lambda) d\lambda. \quad (3)$$

The physical phenomenon of this compressive sensing procedure is shown in Figure 3, where the discrete form of the binary polar coded aperture is written as

$$t_{sr} = \int_{r\Delta_\rho(r)}^{(r+1)\Delta_\rho(r)} \int_{s\Delta_\varphi(r)}^{(s+1)\Delta_\varphi(r)} T(\varphi, \rho) \rho d\varphi d\rho, \quad (4)$$

where s and r index the spokes and rings in the polar coded aperture, respectively. $\Delta_\varphi(r)$ is the pitch of spokes in r^{th} ring, while $\Delta_\rho(r)$ represents the pitch of the r^{th} ring. Denote the integration region of the $(s, r)^{\text{th}}$ polar pixel as Ω_{sr}, then the binary polar coded aperture is rewritten as

$$t_{sr} = \iint_{\Omega_{sr}} T(\varphi, \rho) \rho d\varphi d\rho. \quad (5)$$

The discrete representation of the 3D data cube is written as

$$f_{srk} = \int_{\lambda_k}^{\lambda_{k+1}} \iint_{\Omega_{sr}} f(\varphi, \rho, \lambda) \rho d\varphi d\rho d\lambda. \quad (6)$$

Similarly, the discrete form of the continuous variable circular bandpass filter is represented as

$$c_{srk} = \int_{\lambda_k}^{\lambda_{k+1}} \iint_{\Omega_{sr}} C(\varphi, \lambda) \rho d\varphi d\rho d\lambda. \quad (7)$$

The physical phenomenon of this discrete spectral modulation is illustrated in Figure 4. The modulation amplitude c_{srk} is determined by the center wavelengths and the bandwidth of the bandpass filter. The impact of the bandpass filter bandwidth is further discussed in Section IV.

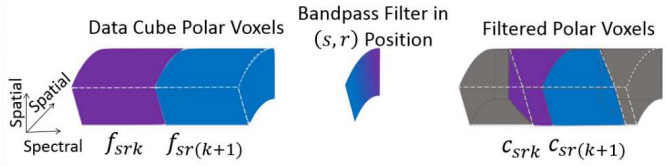

Figure 4. Illustration of the spectral modulation of the filtered polar data cube. Two spectrally adjacent polar data cube voxels are modulated in spectrum as passing through a continuous variable circular bandpass filter pixel.

The continuous change of the center wavelength with the change of the angular position in the circular bandpass filter enables the division of the spectral channels. The spectrum is uniformly divided into L bands from $\lambda_{min} - b_w/2$ to $\lambda_{max} + b_w/2$, where as defined above, $[\lambda_{min}, \lambda_{max}]$ is the center wavelength range of the bandpass filter, and b_w is the filter bandwidth. The spatial and spectral modulated polar data cube is integrated in the spectral domain. The discrete form of this polar projection is

$$\begin{aligned} g_{sr} &= \iint_{\Omega_{sr}} T(\varphi, \rho) \int C(\varphi, \lambda) f(\varphi, \rho, \lambda) d\lambda \rho d\rho d\varphi \\ &= \sum_k \iint_{\Omega_{sr}} T(\varphi, \rho) \int_{\lambda_k}^{\lambda_{k+1}} C(\varphi, \lambda) f(\varphi, \rho, \lambda) \rho d\lambda d\rho d\varphi \\ &= \sum_k t_{sr} c_{srk} f_{srk}. \end{aligned} \quad (8)$$

Denote the vector form of the data cube and the integrated coded scene as $\mathbf{f}$ and $\mathbf{g}_1$, respectively. This sensing process in the ℓ^{th} snapshot can be written in matrix form as

$$\mathbf{g}_1^\ell = \mathbf{P}^\ell \mathbf{f}, \quad (9)$$

where $\mathbf{P}^\ell$ represents the effect of the polar coded aperture and the continuous variable circular bandpass filter. The vector form of the bandpass filter modulation in k^{th} spectral channel is represented as

$$\mathbf{c}_k^\ell = [c_{11k}^\ell, c_{21k}^\ell, ..., c_{12k}^\ell, ..., c_{S_{out}Rk}^\ell]^T. \quad (10)$$

This article has been accepted for publication in a future issue of this journal, but has not been fully edited. Content may change prior to final publication. Citation information: DOI 10.1109/TCI.2016.2617740, IEEE Transactions on Computational Imaging

Similarly, the vector form of the polar coded aperture in the ℓ^{th} snapshot is given by

$$\mathbf{t}^{\ell} = [t^{\ell}_{11}, t^{\ell}_{21}, ..., t^{\ell}_{12}, ..., t^{\ell}_{S_{out}R}]^T. \quad (11)$$

Then the coding matrix $\mathbf{P}^{\ell}$ is written as

$$\mathbf{P}^{\ell} = [\text{diag}(\mathbf{t}^{\ell} \circ \mathbf{c}^{\ell}_1), \text{diag}(\mathbf{t}^{\ell} \circ \mathbf{c}^{\ell}_2), ..., \text{diag}(\mathbf{t}^{\ell} \circ \mathbf{c}^{\ell}_{\text{L}})], \quad (12)$$

where $\mathbf{t}^{\ell} \circ \mathbf{c}^{\ell}_k$ is the element-wise product of $\mathbf{t}^{\ell}$ and $\mathbf{c}^{\ell}_k$. Denote the total number of polar pixels in the coded aperture as $V = R_{in}S_{in} + R_{out}S_{out}$. Then $\mathbf{P}^{\ell}$ has the dimensions of $V \times VL$. In order to visualize $\mathbf{P}^{\ell}$, a test data cube with 2 inner rings ($R_{in} = 2$), 8 inner spokes ($S_{in} = 8$), 1 outer rings ($R_{out} = 1$), 16 outer spokes ($S_{out} = 16$), and 2 spectral channels ($L = 2$) is applied. The corresponding $\mathbf{P}^{\ell}$ generated via Eq. (12) is displayed in Figure 5. The gray scale values are between 0 and 1. 80% unblocked pixels are randomly distributed in the polar coded aperture for better demonstration of the CVF modulation $\mathbf{c}^{\ell}_k$ in $\mathbf{P}^{\ell}$. Each spectral band is organized from inner to outer rings, with the spokes in each ring arranged from angles 0 to 2π. In this two band example, the CVF acts as a low pass filter for the first spectral band, and a high pass filter for the second spectral band. This can be observed by the spoke values of the first spectral band falling off from 1 to 0, while the spoke values in the second spectral band increase from 0 to 1.

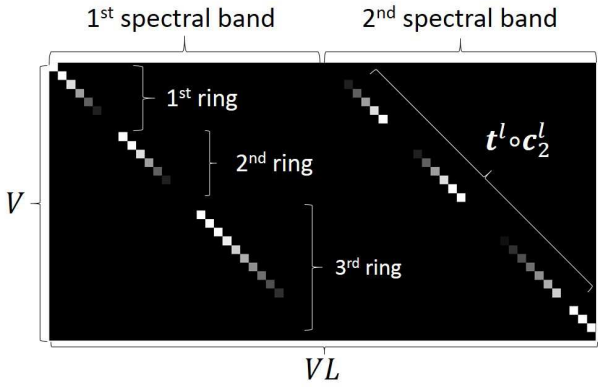

Figure 5. Coding matrix $\mathbf{P}^{\ell}$ for $S_{in} = 8$, $S_{out} = 16$ $R_{in} = 2$, $R_{out} = 1$, $L = 2$ data cube. The entries represent the spatial and spectral modulation factors on the polar data voxels, with 0 entries remaining black.

C. Discussion on the Spectral Resolution

As displayed in the $\mathbf{P}^{\ell}$ image, distinct spectral modulation $\mathbf{c}^{\ell}_k$ for each band k enables the separation of the spectral bands. One spectral band k can always be separated into two or more sub-bands k_i when the spectral modulations $\mathbf{c}^{\ell}_{k_i}$ are different. It is thus possible to separate a band into two sub-bands with distinct spectral coding. Thus, an infinite number of spectral bands could be recovered in principle. As shown in Figure 6, the region $\mathbf{R}^{\ell}_k = \{(s,r)|c^{\ell}_{srk} \neq 0\}$ is the spatial area where the k^{th} spectral band is sensed by the continuous variable filter. Assume this spectral band is uniformly divided into two sub-bands k_1 and k_2. Thus, denote $\mathbf{R}^{\ell}_{k_1} = \{(s,r)|c^{\ell}_{srk_1} \neq 0\}$ and $\mathbf{R}^{\ell}_{k_2} = \{(s,r)|c^{\ell}_{srk_2} \neq 0\}$. Since the bandpass wavelengths differ for different angular positions in the spatial domain, $\mathbf{R}^{\ell}_{k_1} \neq \mathbf{R}^{\ell}_{k_2}$ when the number of spectral bands $L \leq S_{out}$. Then, there exists a polar pixel (s_1, r_1), such that $(s_1, r_1) \in \mathbf{R}^{\ell}_{k_1}$ and $(s_1, r_1) \notin \mathbf{R}^{\ell}_{k_2}$. Similarly, another polar pixel (s_2, r_2) exists, such that $(s_2, r_2) \in \mathbf{R}^{\ell}_{k_2}$ and $(s_2, r_2) \notin \mathbf{R}^{\ell}_{k_1}$. Therefore, the following equations hold,

$$\begin{cases} c^{\ell}_{s_1 r_1 k_1} \neq 0 \\ c^{\ell}_{s_1 r_1 k_2} = 0 \end{cases} \text{ and } \begin{cases} c^{\ell}_{s_2 r_2 k_1} = 0 \\ c^{\ell}_{s_2 r_2 k_2} \neq 0 \end{cases}, \quad (13)$$

resulting in $\mathbf{c}^{\ell}_{k_1} \neq \mathbf{c}^{\ell}_{k_2}$. Thus, the two sub-bands k_1 and k_2 are separated.

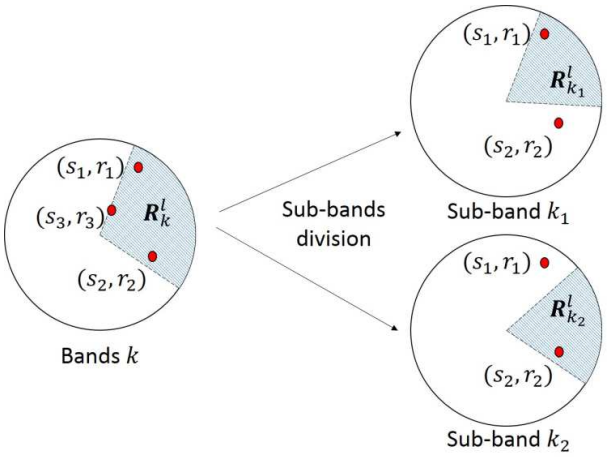

Figure 6. The polar pixels in k^{th} spectral band that can be sensed by the continuous variable filter are concentrated in the region of $\mathbf{R}^{\ell}_k$. This spectral band is split into two sub-bands where the sensed polar pixels are concentrated in two smaller regions $\mathbf{R}^{\ell}_{k_1}$ and $\mathbf{R}^{\ell}_{k_2}$.

In the situations that $L > S_{out}$, $\mathbf{R}^{\ell}_{k_1} = \mathbf{R}^{\ell}_{k_2} = \mathbf{R}^{\ell}_k$. For any polar pixel (s_3, r_3) located in the edges of $\mathbf{R}^{\ell}_{k_1}$, $c^{\ell}_{s_3 r_3 k_1} \neq c^{\ell}_{s_3 r_3 k_2}$. Thus $\mathbf{c}^{\ell}_{k_1} \neq \mathbf{c}^{\ell}_{k_2}$. The two sub-bands k_1 and k_2 can still be distinguished by the imager.

However, notice from Figure 6 that in each single snapshot, amounts of elements in both $\mathbf{c}^{\ell}_{k_1}$ and $\mathbf{c}^{\ell}_{k_2}$ are 0, making it impossible to recover either k_1 or k_2 band in the corresponding spatial area. Thus, a number of imager rotations are needed to modulate a certain spatial area with the whole spectrum of the bandpass filter. In consequence, an infinite number of spectral bands could be separated with unlimited number of shots, under the conditions that the bandpass filter ideally changes its center wavelength continuously along the angular positions.

In addition, as discussed in Section IV, a larger number of reconstructed spectral bands requires a narrower bandwidth of the bandpass filter to achieve the best recovery performance. In Section IV. D, a 11.6nm wide bandpass filter is applied for a successful reconstruction of 128 bands, where $L = 2S_{out}$. Narrower bandwidths are more difficult to manufacture. Moreover, the difficulties for the spectral modulation calibration process also increase with $L > S_{out}$. All these practical difficulties need to be considered for the real implementation of the proposed imager.

D. Sensing Model of the Rectangular FPA sensors

The FPA detector consists of N^2 rectangular sensors. Denote the Cartesian representation of the FPA projection as

$g_c(x,y)$. Then $g_c(\rho\cos\varphi, \rho\sin\varphi) = g_p(\varphi,\rho)$. The discrete FPA pixel measurement is

$$g_{mn} = \int_{n\Delta_c}^{(n+1)\Delta_c} \int_{m\Delta_c}^{(m+1)\Delta_c} g_c(x,y)dxdy, \tag{14}$$

where Δ_c is the square FPA pixel pitch. Denote the integration region of $(m,n)^{th}$ pixel as D. Then the discrete FPA measurement is

$$\begin{aligned} g_{mn} &= \iint_{D_{mn}} g_c(x,y)dxdy \\ &= \iint_{D_{mn}} g_p(\varphi,\rho)\rho d\rho d\varphi. \end{aligned} \tag{15}$$

With the forward model expressed in Eq. (3) and Eq. (8), the FPA measurement is represented as

$$\begin{aligned} g_{mn} &= \iint_{D_{mn}} T(\varphi,\rho)\int C(\varphi,\lambda)f(\varphi,\rho,\lambda)d\lambda\rho d\rho d\varphi \\ &= \sum_r\sum_s w_{srmn}\int_{r\Delta_\rho(r)}^{(r+1)\Delta_\rho(r)}\int_{s\Delta_\varphi(r)}^{(s+1)\Delta_\varphi(r)} T(\varphi,\rho) \\ &\quad \int_{\lambda_{min}-b_w/2}^{\lambda_{max}+b_w/2} C(\varphi,\lambda)f(\varphi,\rho,\lambda)\rho d\lambda d\rho d\varphi \\ &= \sum_r\sum_s w_{srmn}g_{sr}, \end{aligned} \tag{16}$$

where w_{srmn} is the proportion of the energy in the $(s,r)^{\text{th}}$ polar coded aperture pixel sensed by the $(m,n)^{\text{th}}$ FPA sensor, given by

$$w_{srmn} = \iint_{D_{mn}\cap\Omega_{sr}} \rho d\rho d\varphi \Big(\iint_{\Omega_{sr}} \rho d\rho d\varphi\Big)^{-1}. \tag{17}$$

Denote the vector form of the ℓ^{th} shot measurements as $\mathbf{g}^\ell$. Then this polar-rectangular transformation can be expressed in matrix form as

$$\mathbf{g}^\ell = \mathbf{W}^\ell\mathbf{g}_1^\ell, \tag{18}$$

where $\mathbf{W}^\ell$ has the dimensions of $N^2\times V$. Then $\mathbf{W}^\ell$ accounts for the weights w_{srmn} of the polar coded aperture sensed on $N\times N$ FPA sensors. Thus, the $(i,j)^{\text{th}}$ entry of $\mathbf{W}^\ell$ is $W_{ij}^\ell = w_{pquv}$, where $v = \left\lfloor \frac{i}{N} \right\rfloor$ indexes the number of FPA columns, and $u = i - vN$ counts the number of FPA rows; Similarly,

$$q = \begin{cases} \left\lfloor \frac{j}{S_{in}} \right\rfloor, & \text{if } j \le S_{in}R_{in} \\ R_{in} + \left\lfloor \frac{j-S_{in}R_{in}}{S_{out}} \right\rfloor, & \text{otherwise} \end{cases} \tag{19}$$

indexes the polar coded aperture rings, and

$$p = \begin{cases} j - qS_{in}, & \text{if } j \le S_{in}R_{in} \\ j - R_{in}S_{in} - (q-R_{in})S_{out}, & \text{otherwise} \end{cases} \tag{20}$$

counts the spokes of the polar coded aperture.

In order to visualize $\mathbf{W}$, the same test data cube used in Figure 5 is applied here. The FPA is assumed to have 4 by 4 sensors ($N^2 = 4^2$). The corresponding weight matrix $\mathbf{W}$ is shown in Figure 7.

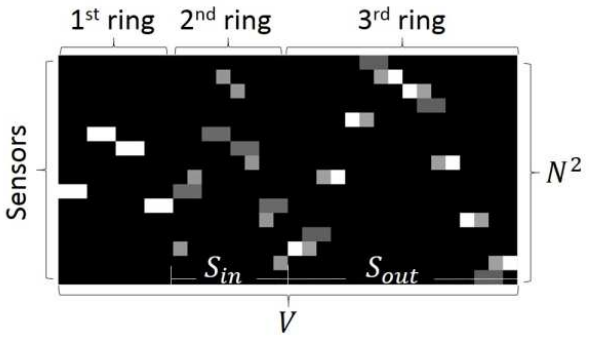

Figure 7. Weight matrix $\mathbf{W}$ for a $S_{in} = 8$, $S_{out} = 16$ $R_{in} = 2$, $R_{out} = 1$, $L = 2$ data cube and an $N^2 = 4^2$ FPA. The entries with larger values are displayed in brighter points, while the 0 entries remain black.

E. Sensing Matrix of Discrete Rotation Model

By combining Eq. (8) and Eq. (16), the FPA measurement in ℓ^{th} snapshot is

$$g_{mn}^\ell = \sum_r\sum_s\sum_k w_{srmn}^\ell t_{sr}^\ell c_{srk}^\ell f_{srk}, \tag{21}$$

Similarly, from Eq. (9) and Eq. (18), the matrix representation of the sensing procedure is expressed as

$$\begin{aligned} \mathbf{g}^\ell &= \mathbf{W}^\ell\mathbf{P}^\ell\mathbf{f} \\ &= \mathbf{H}^\ell\mathbf{f}, \end{aligned} \tag{22}$$

where $\mathbf{H}^\ell = \mathbf{W}^\ell\mathbf{P}^\ell$ is the sensing matrix for the ℓ^{th} shot. Applying the same test data in Figure 5 and Figure 7, $\mathbf{H}^\ell$ can be visualised in Figure 8.

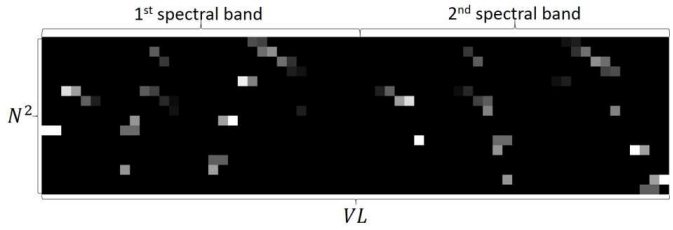

Figure 8. Sensing matrix $\mathbf{H}^\ell$ for a $S_{in} = 8$, $S_{out} = 16$ $R_{in} = 2$, $R_{out} = 1$, $L = 2$ data cube and an $N^2 = 4^2$ FPA.

Let K-snapshot measurements be represented in the vector form $\mathbf{g} = [(\mathbf{g}^1)^T, (\mathbf{g}^2)^T, ..., (\mathbf{g}^K)^T]^T$. Then the sensing procedure is written as $\mathbf{g} = \mathbf{Hf}$, where $\mathbf{H} = [(\mathbf{H}^1)^T, (\mathbf{H}^2)^T, ..., (\mathbf{H}^K)^T]^T$. The relationship between the sensing procedures in different snapshots is further analysed. The imager rotation motion enables multiple snapshots measurements embedded with different spatial and spectral coding. If the imager rotation exceed 2π, the patterns of polar coded aperture and the circular bandpass filter repeats themselves, resulting in duplicated measurements. Thus the number of snapshots is restricted to the coded aperture design. As will be shown in Section III, a good geometry design of the coded aperture has fewer spokes in the inner rings than the outer rings, i.e, $S_{in} < S_{out}$. Thus the maximum number of snapshots captured is limited by the number of spokes in the polar coded aperture inner rings, $K \le S_{in}$.

This article has been accepted for publication in a future issue of this journal, but has not been fully edited. Content may change prior to final publication. Citation information: DOI 10.1109/TCI.2016.2617740, IEEE Transactions on Computational Imaging

Assume the polar coded aperture rotates d_r pixels in the r^{th} ring between adjacent snapshots acquired and assume K snapshots are taken within the rotation period τ_r, then, d_r is represented as

$$d_r = \left\lfloor \frac{S_r}{K} \right\rfloor, \tag{23}$$

where S_r is the number of spokes in r^{th} ring. As shown in Figure 9, the spatial coding provided by the coded aperture has a circular shift in its spokes between snapshots.

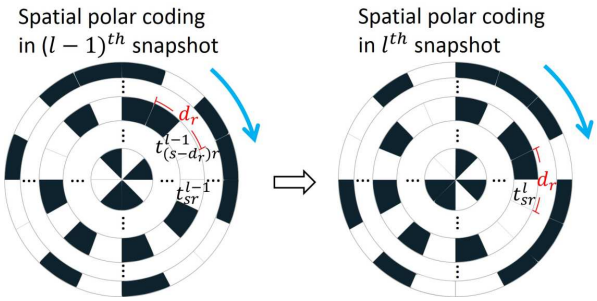

Figure 9. As the imager rotates, the spatial coding provided by the polar coded aperture is circularly shifting the spokes. The imager is assumed to be static when snapshots are captured, and d_r spokes are shifted between adjacent shots.

Then the current snapshot coded aperture can be obtained from the previous shot coded aperture as

$$t^{\ell}_{sr} = \begin{cases} t^{\ell-1}_{s-d_r,r}, & \text{if } r \le d_r \\ t^{\ell-1}_{s+S_r-d_r,r}, & \text{otherwise.} \end{cases} \tag{24}$$

A permutation matrix $\mathbf{M}$ can represent this circular shift procedure, with the ℓ^{th} shot coded aperture calculated as

$$\mathbf{t}^{\ell} = \mathbf{M}\mathbf{t}^{\ell-1}. \tag{25}$$

Similarly, the spectrum modulation of each spectral band performs the same spokes shift between snapshots. Thus the ℓ^{th} shot spectrum modulation is calculated as

$$\mathbf{c}^{\ell}_{k} = \mathbf{M}\mathbf{c}^{\ell-1}_{k}. \tag{26}$$

$\mathbf{P}^{\ell}$ can be constructed by applying Eq. (11). Notice that the columns of $\mathbf{W}^{\ell}$ are organized in the same fashion as the polar coded aperture structure, performing the same permutation procedure. Then the transformation of $\mathbf{W}^{\ell}$ between adjacent snapshots is modelled as

$$(\mathbf{W}^{\ell})^T = \mathbf{M}(\mathbf{W}^{\ell-1})^T. \tag{27}$$

F. Spectral Data Cube Recovery

Since the polar coded aperture pixels share the same pixel size, the desired polar image band can be organized into rectangular matrix as shown in Fig 10. The inner-ring matrix with the dimension of $S_{in}\times R_{in}$ is the matrix formulation of the inner rings polar pixels. Similarly, the outer rings polar pixels are transformed into a $S_{out}\times R_{out}$ rectangular matrix.

Then a Kronecker basis $\mathbf{\Psi} = \mathbf{\Psi}_1 \otimes \mathbf{\Psi}_2 \otimes \mathbf{\Psi}_3$ is applied to the matrix cubes, where $\mathbf{\Psi}_1 \otimes \mathbf{\Psi}_2$ provides the basis in the spatial domain and $\mathbf{\Psi}_3$ is the basis in the spectral domain.

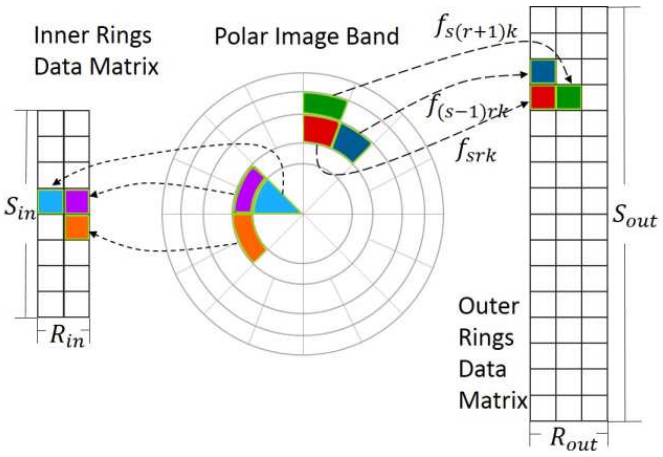

Figure 10. One polar image band is transformed into two rectangular matrices representing the inner and outer rings polar image pixels.

Thus the polar data cube $\mathbf{f}$ is represented as $\mathbf{f} = \mathbf{\Psi}\boldsymbol{\theta}$. In the simulation, we apply the Kronecker product of the 2D Wavelet in space and 1D discrete cosine transform (DCT) in spectrum as the basis, which has been shown as an efficient sparse basis in compressive spectral imaging [19,32,33]. Instead of the DCT, other bases such as the Wavelet transform along the spectral axis could be applied [33-36]. A further research could focus on optimizing the basis representation for polar spectral images. Then the sensing process can be expressed in Eq. (2). The signal reconstruction is then performed by solving the inverse problem of the underdetermined linear system, where $\boldsymbol{\theta}$ is recovered to minimize a l_1-l_2 cost function. This signal recovery problem is expressed as

$$\hat{\boldsymbol{\theta}} = \arg\min_{\boldsymbol{\theta}} \|\mathbf{g} - \mathbf{A}\boldsymbol{\theta}\|^2 + \lambda|\boldsymbol{\theta}|_1, \tag{28}$$

where λ is a regularization constant. In the simulation, the gradient projection for sparse reconstruction (GPSR) algorithm [37] is applied. In Matlab R2011b and a computer with the Intel(R) Core(TM) i7 CPU and 6.00GB RAM, the reconstruction algorithm takes approximate 447 seconds to recover a 16-band data cube with 128^2 spatial resolution in 600 iterations. Note the reconstruction speed can be significantly improved by performing code optimization, applying parallel computing or simply alternating the reconstruction algorithm.

III. Polar Coded Aperture Geometry Design

The polar coded aperture rotates together with the proposed imaging system, providing a set of block-unblock coded measurements to the detector. Thus the scene is sampled according to the polar geometry of the rotating aperture, resulting in polar shaped image pixels. The geometry design of the polar coded aperture aims at improving the image sensing strategy.

Similar structures of polar images have been proposed with the name of "log-polar image" in the field of computer vision [38,39]. The concept of polar pixels has also been applied in CT [40], SPECT [41,42], Compton SPECT [43], and PET [44]. Our design of the polar coded aperture takes the advantages of the spokes-rings structure, as shown in Figures 11 (a) and (b). This structure transforms the image

rotation motion directly into a circularly shift of the polar pixels. The proposed imaging system aims at obtaining a uniform spatial resolution across the scene. Uniformly sensing is achieved by designing the spaces between rings, resulting in a projection where the same pixel size is attained across the image.

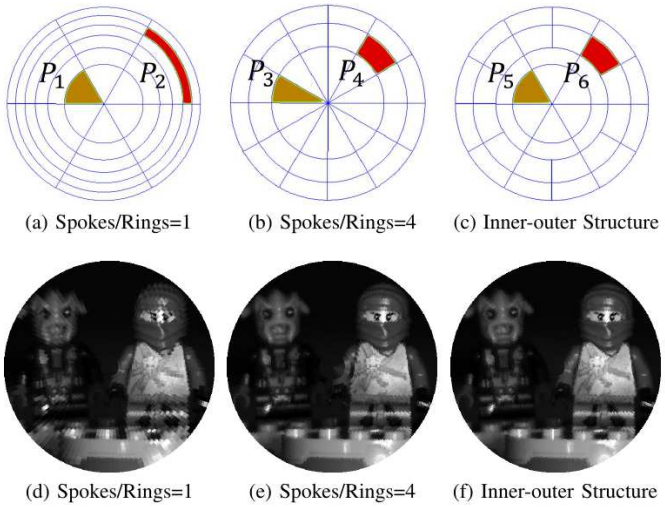

Figure 11. (a)-(c) show different polar aperture geometry designs with the shapes polar pixels being analysed: (a) and (b) show the spoke-ring aperture structure with $S/R = 1$ and $S/R = 4$, respectively; (c) shows the inner-outer rings design. (d)-(f) are the examples of polar images with the corresponding polar pixels geometry in (a)-(c), respectively.

Denote R and S as the number of rings and spokes, respectively. Figures 11 (a) and (b) show the influence of the spoke-ring ratio S/R to the image quality: Higher density of rings leads to good image quality in the inner rings, while higher density of spokes leads to good image quality in the outer rings. To determine the optimal spoke-ring ratio S/R, an analysis of the pixel shape is shown in Figure 11 (a)-(b), where the pixels P_2 and P_3 are highly unbalanced in the lengths of their rings and spokes, resulting in a poor image quality. On the other hand, pixels P_1 and P_4 have similar rings and spokes lengths, resulting in a more balanced sensing along both dimensions which is desired in the geometry design. Denote the widths between the rings and the spokes in $(s, r)^{\text{th}}$ pixel as a_{sr} and b_{sr}, respectively, as shown in Figure 12, where s indexes the spokes and r counts the rings. The design principle is to achieve a minimum difference between a_{sr} and b_{sr} for each pixel. Thus, a sum of the squared differences between a_{sr} and b_{sr} across all s and r is calculated as a cost function, expressed as

$$\text{Cost} = \sum_{\text{r}} \sum_{\text{s}} (\text{a}_{\text{sr}} - \text{b}_{\text{sr}})^2. \tag{29}$$

Then the cost values are computed for different S/R ratio, as displayed in Figure 13. $S/R = 4$ provides the minimal cost value. However, since the cost function only minimizes an average value, polar images with $S/R = 4$ still have unbalanced pixel shapes in the inner rings as shown in Figure 11 (b). Instead, the aperture with $S/R = 1$ provides more balanced pixel shapes in the inner rings as shown in Figure 11 (a). However, it suffers from unbalance pixel shapes in outer rings,

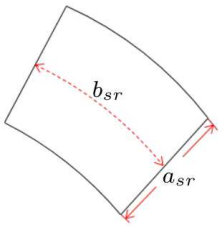

Figure 12. The shape of a polar pixel with rings distance a_{sr} and spokes distance b_{sr}.

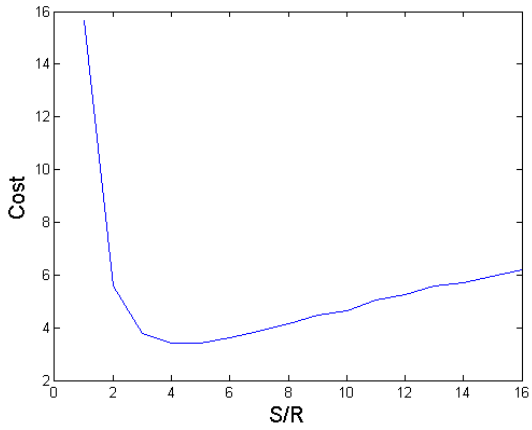

Figure 13. Plot of the cost function value changing with the spoke-ring ratio S/R varying from 1 to 16.

resulting in a higher value of the cost function. The aperture with a fixed ratio of S/R can not provide good image quality in all spatial positions of the scene. Thus, a new geometry design of the polar aperture is proposed to have an inner-outer ring structure that is shown in Figure 11 (c). The new design keeps the spokes-rings structure with $S/R = 4$ in the outer rings, while reducing the number of the spokes in the inner rings to improve the overall image quality. The number of spokes in the inner rings is half of the spokes number in the outer rings, denoted as $S_{in} = 0.5S_{out}$, which results in a higher density of rings in the inner rings and a higher density of spokes in the outer rings. As shown in Figure 11 (d)-(f), the image quality is improved with the new design.

The inner-outer ring structure can be further designed by determining the inner-total rings ratio, defined as $\varepsilon = R_{in}/(R_{in} + R_{out})$. A proper value of ε is desired such that the cost function expressed in Eq. (29) is minimized. Figure 14 shows the cost function value changing with the variable ε when the numbers of inner spokes S_{in} are 128 and 256 respectively, with the constrain that the total number of polar coded aperture pixels remains S_{in}^2. The values for ε between 0.2 to 0.3 result in smaller cost values, with the minima at $\varepsilon = 0.27$ for both $S_{in} = 128$ and $S_{in} = 256$ cases, with corresponding $R_{in} = 20$ and $R_{in} = 40$, respectively.

This result is verified by showing an image quality comparison with 6, 20, and 60 inner rings (with the corresponding $\varepsilon = 0.09, 0.27$ and 0.64), as shown in Figure 15. In this comparison, the number of pixels are fixed as $S_{in}^2 = 128^2$.

This article has been accepted for publication in a future issue of this journal, but has not been fully edited. Content may change prior to final publication. Citation information: DOI 10.1109/TCI.2016.2617740, IEEE Transactions on Computational Imaging

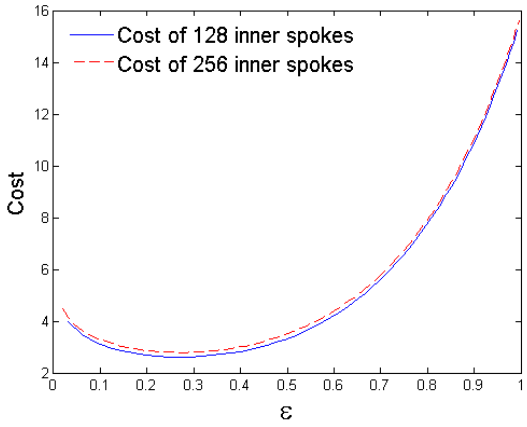

Figure 14. Plots of the cost function value changing with the inner-total rings ratio $\varepsilon \in [0, 1]$ in both 128 inner spokes and 256 inner spokes coded apertures.

With two regions on the eyes and chest of the toy zoomed, it is clear that the image sampled by a $R_{in} = 20$ polar aperture obtains better image quality in both areas.

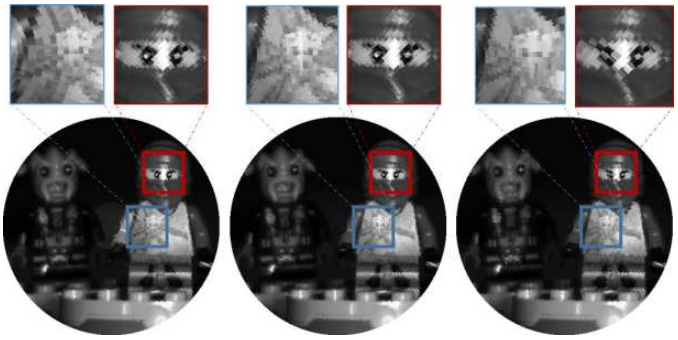

Figure 15. Comparison of image quality with 6 (left), 20 (middle) and 60 (right) inner rings with the polar pixel number restricted to be 128^2. Better image quality with 20 inner rings is observed in both zoomed regions.

IV. Computer Simulations

A. Polar Data Cube Acquisition and Measurements Simulation

To further study the proposed imaging system, computer simulations are performed with a polar spectral data cube acquired in the laboratory. A wide-band Xenon lamp is used as the light source and a visible monochromator is applied to capture spectral bands on a 9.9μm CCD camera. In this way, a 256×256×16 data cube is obtained. Then, the acquired data cube is transformed into a polar data cube with 20 inner rings and 54 outer rings by software. The numbers of spokes are 128 and 256 in the inner and outer rings, respectively. Fig 16 shows the 9 polar spectral image bands selected from the total $L = 16$ bands. The center wavelengths of each spectral channel are uniformly distributed in the range from 451nm to 661nm.

In the simulation, the polar coded aperture has $R_{in} = 20$ inner rings and $R_{out} = 54$ outer rings. $S_{in} = 128$ and $S_{out} = 256$ spokes are uniformly spaced in the inner rings and outer rings, respectively. A random binary code with 50%

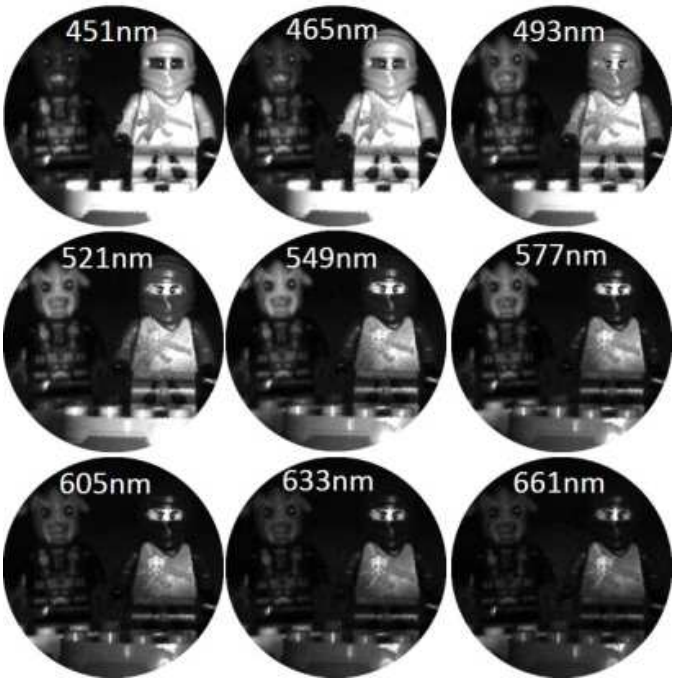

Figure 16. 9 spectral image bands selected from the total 16 bands are displayed. The center wavelength of each band is indicated. Two image points are selected for the spectral reconstruction comparisons.

open is applied on the polar coded aperture. The continuous variable circular bandpass filter is simulated with the center wavelengths ranging from 476nm to 635nm. The bandwidth is assumed to be 80nm. Meanwhile, a $N^2 = 32^2$ FPA sensor is utilized to capture the compressed projections. Then the compressive sensing ratio (CS ratio) of K snapshots measurements is defined as

$$\kappa = \frac{KN^2}{VL}, \tag{30}$$

where $V = S_{in}R_{in} + S_{out}R_{out}$.

By applying Eq. (21), 64 snapshots measurements are simulated, where the CS ratio is $\kappa = 25\%$. In order to show the simulation process, Figure 17 (a) displays the RGB images of the spatial and spectral modulated polar data cube before being projected on the FPA. The RGB images demonstrate the aperture coding and CVF spectral modulation to the scene. The spatial resolution of each RGB image is 128^2. The corresponding simulated compressed projections are displayed in Figure 17 (b), demonstrating the spatial and spectral integration on the low resolution monochromatic FPA. The spatial resolution of these FPA projections is 32^2.

B. Reconstruction with Simulated Measurements

The reconstruction procedure applies the GPSR algorithm to solve the $\ell_1 - \ell_2$ function described in Eq. (28), where the representation basis utilizes a 2D Wavelet basis and a 1D Cosine basis in the spatial and spectral domains, respectively. Peak signal to noise ratio (PSNR) is calculated for each reconstructed spectral channel.

This article has been accepted for publication in a future issue of this journal, but has not been fully edited. Content may change prior to final publication. Citation information: DOI 10.1109/TCI.2016.2617740, IEEE Transactions on Computational Imaging

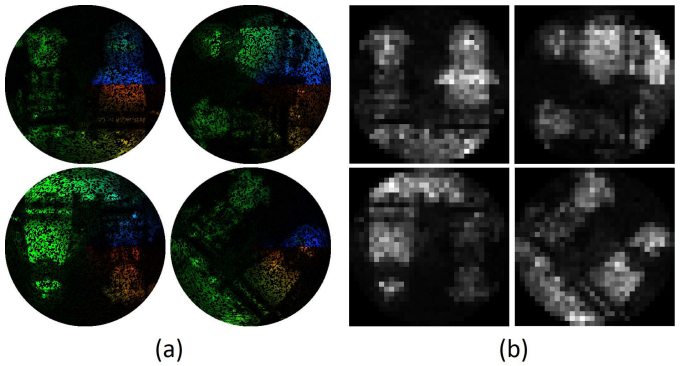

Figure 17. (a) shows the RGB images of the spatial and spectral modulated polar data cube before projected on the FPA detector. (b) shows the corresponding compressed FPA projections. 4 snapshots selected from the total 64 snapshots are displayed.

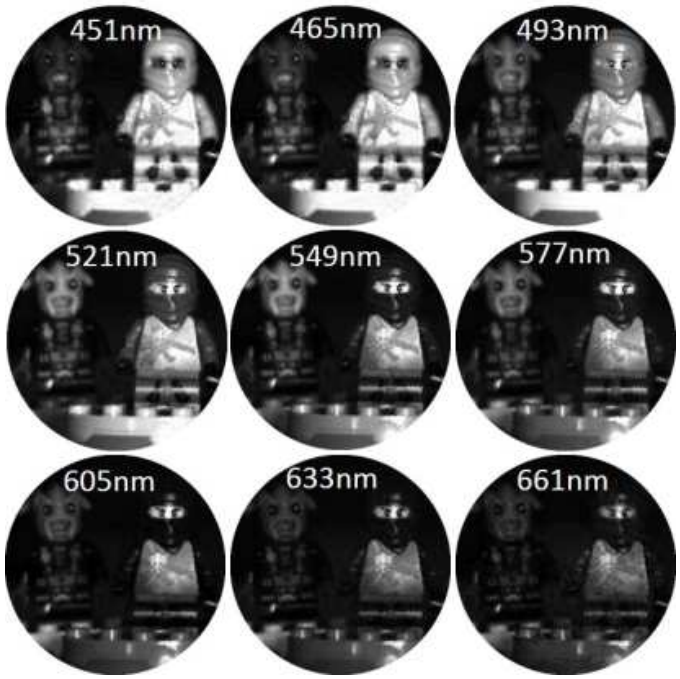

Figure 18. 16 spectral image bands are reconstructed from 64 snapshots compressed measurements with $\kappa = 25\%$ CS ratio, where 9 image bands are displayed. The average PSNR is 32dB.

Figure 18 shows 9 image bands selected from the reconstructed 16 spectral bands. The average PSNR is 31.8dB. Good image quality is observed in the reconstructed spectral bands. With a larger number of snapshots captured, more information of the polar data cube is acquired, with a higher reconstruction accuracy expected. Thus, simulations are performed with different numbers of snapshots applied in the reconstruction. The PSNRs of the reconstructions are calculated and displayed in Figure 19. The simulation results verify the performance improvement by increasing the number of snapshots. Note that the maximum number of snapshots is limited by the number of spokes in inner rings, which has a CS ratio of 50%. The spokes-rings coded aperture structures with $S/R = 1$ and $S/R = 4$ have similar reconstruction performance compared with the inner-outer ring coded aperture in Figure 19. This is not surprising since the geometry design of the polar coded aperture aims at better image quality instead of better reconstruction performance. The reconstruction quality could be improved by further optimizing the aperture code patterns.

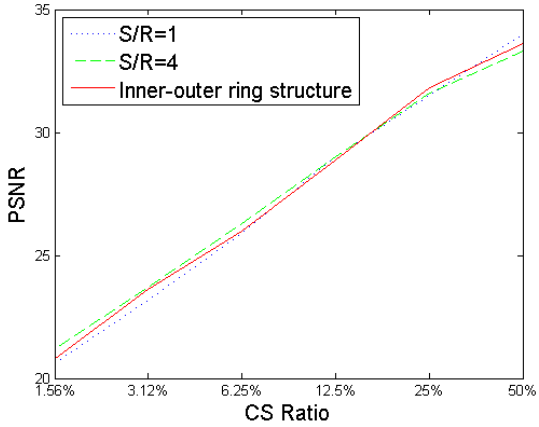

Figure 19. Average PSNRs are calculated for different polar coded aperture geometry designs with the number of snapshots ranging from 4 to 128. The corresponding CS ratio ranges from 1.56% to 50%.

Note that a random coded aperture with 50% open can generally produce better reconstruction in polar coded aperture compressive sensing imaging. In this simulation, the performance decreases by 0.6dB PSNR if the transmittance is decreased to 30%. When the transmittance increases to 80%, a PSNR reduction of 0.8dB is observed. The FPA resolution influences the reconstruction quality. A higher resolution FPA performs slightly better, due to the additional spatial measurements per snapshot and better spectral bands differentiation. For example, the reconstruction from 8 shots in a 64^2 FPA is 0.6dB better than the reconstruction from 128 shots in a 16^2 FPA. However, we should also point out that the reconstruction performance is determined by all hardware configurations including the FPA resolution, the CVF bandwidth and the coded aperture patterns. In addition, higher resolution FPAs are typically more costly, particularly in the IR bands.

Sensor noise can also influence the reconstruction performance. Here we define the signal-to-noise ratio (SNR) in the sensor as the ratio between the variance of the sensor measurements and the variance of sensor noise, $\text{SNR} = 10\log_{10}\text{Var}(\mathbf{g})/\text{Var}(\mathbf{n})$, where $\mathbf{n}$ represents the noise. When Gaussian white noise resulting in 30dB, 20dB and 10dB SNR is added to the measurements, the resulting PSNR decreases 2dB, 5dB and 8dB, respectively. The optimal choice of the regularization parameter τ in Eq. (28) tends to be larger with stronger noise, indicating that more effort is needed in ℓ_1 minimization for a smooth image recovery. The robustness can be improved by employing alternative optimization algorithms with noise reduction.

C. Influence of the Bandpass Filter Bandwidth

The bandwidth and the range of the center wavelengths of the continuous variable bandpass filter have a great impact on

the values of the spectrum modulation c^{ℓ}_{srk}, which eventually influence the sensing matrix $\mathbf{H}$ and the reconstruction quality. Generally, if the bandwidth of the bandpass filter is too narrow, not enough of the spectral information is compressively sensed, causing poor reconstructions. Meanwhile, if the bandwidth is too wide to provide distinct modulation for different spectral bands, the proposed imager will fail in the spectral reconstruction.

To study this influence, a data cube with 128 spectral bands is applied in the measurements simulation procedure, where the high spectral resolution results in a more precise simulation of the continuous variable bandpass filter. Simulations are performed with a varying ratio $\gamma = b_w/(\lambda_{max} - \lambda_{min})$ between the bandwidth b_w and the center wavelengths range $\lambda_{max} - \lambda_{min}$, while keeping the total transmitted wavelength range $[\lambda - b_w/2, \lambda + b_w/2]$ fixed. 8, 16 and 32 spectral bands are reconstructed respectively. PSNRs are calculated with γ ranging from 0.02 to 1 as shown in Figure 20. With the

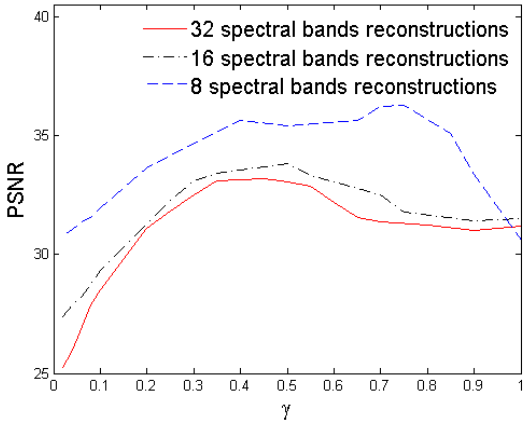

Figure 20. PSNRs of 8, 16 and 32 spectral bands reconstructions from 64 snapshots are displayed with γ varying from 0.02 to 1.

extreme values of $\gamma = 0.02$ or $\gamma = 1$, poor reconstructions are acquired as expected. However, the best values of γ gradually decrease from 0.75 to 0.35 when the number of recovered spectral bands increases from 8 to 32, indicating that a narrower bandpass filter is preferred when a higher spectral resolution is desired.

D. Hyper-Spectral Reconstruction

For further verification of the spectral reconstruction attained, simulations aim at accurate spectral reconstruction with a large number of spectral bands. A 128 bands data cube is used with a spatial resolution of 32^2 polar pixels. The 580nm image band is shown in Figure 21 (a), where two image points are selected for spectral signature comparisons.

With a 32^2 resolution FPA detector, 32 snapshots are simulated, where the CS ratio defined in Section IV. A is $\kappa = 25\%$. As discussed above, the reconstruction of a larger number of spectral bands requires a continuous variable filter with a narrower bandwidth. For 128 spectral bands reconstruction, a 11.6nm bandwidth is selected and applied in the simulation, with the corresponding $\gamma = 0.1$. The reconstruction achieves

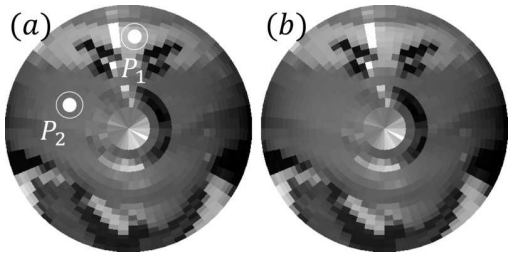

Figure 21. The original 580nm image plane (a) and its corresponding reconstruction (b) are displayed. 40dB PSNR is achieved with $\kappa = 25\%$. Two image points are selected for spectral signature reconstruction comparisons.

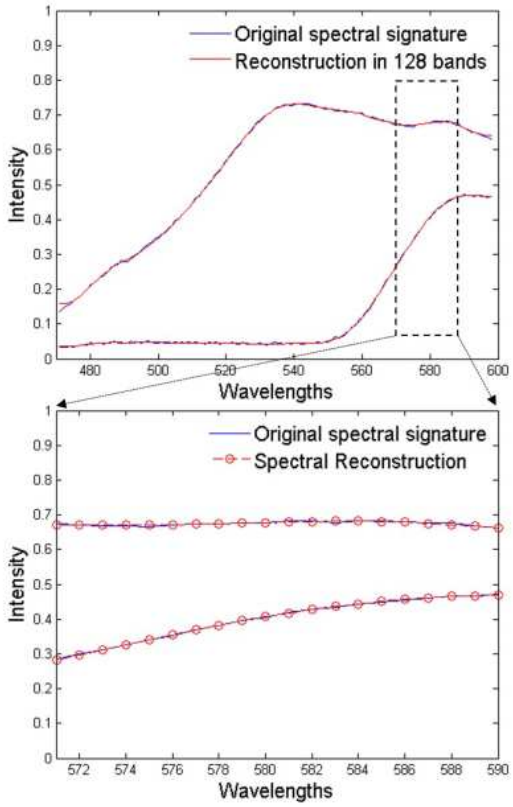

Figure 22. 128-band spectral reconstructions are compared with the original spectral signatures of two image points. The reconstructions of 20 bands from 571nm to 590nm are zoomed for further comparisons.

an average of 40dB PSNR, with the reconstructed 580nm image plane displayed in Figure 21 (b). The reconstruction of spectral signatures in 128 bands are displayed in Figure 22. The spectrum region between 571nm and 590nm containing 20 bands is zoomed for a detailed comparison. The spectral reconstructions of both points are quite close to the original spectral signatures, showing an accurate hyper-spectral recovery.

V. Continuous Imager Rotation Model

For the proposed imager to be mounted on spinning devices, a more precise sensing model is developed by considering the continuous rotation motion. When the continuous rotation is taken into account, the polar pixels in the data cube shears

This article has been accepted for publication in a future issue of this journal, but has not been fully edited. Content may change prior to final publication. Citation information: DOI 10.1109/TCI.2016.2617740, IEEE Transactions on Computational Imaging

circularly during the integration time (or the shutter time) τ_s, as shown in Figure 23.

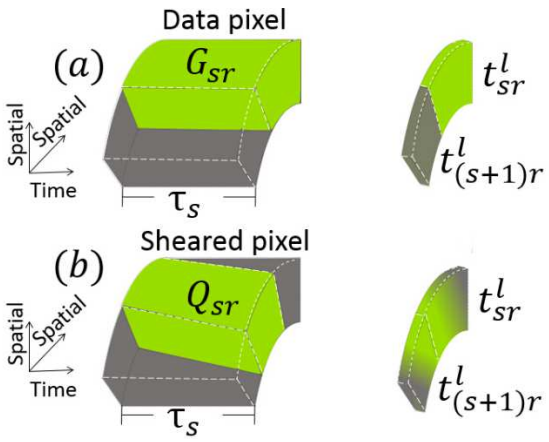

Figure 23. (a) shows a data pixel entering the polar coded aperture with no transformation, when the discrete approximation of the imager rotation is applied. (b) displays a circularly sheared data pixel hitting two adjacent polar aperture pixels, when the continuous rotation motion of the imager is considered.

From the figure, denote the region of the original polar pixel during the time τ_s as G_{sr}; and denote the sheared pixel region during τ_s as Q_{sr}. Then the proportions of the $(s,r)^{\text{th}}$ shear data pixel entering into the polar coded aperture pixels are calculated as

$$\beta_{sru} = \Big(\iiint_{Q_{sr}\cap G_{(s+u)r}} \rho d\rho d\varphi dt\Big)\Big(\iiint_{Q_{sr}} \rho d\rho d\varphi dt\Big)^{-1}, \quad (31)$$

where u indexes the adjacent polar aperture pixels hit by the $(s,r)^{\text{th}}$ sheared data pixel. The sum of the proportions satisfies $\sum_u \beta_{sru} = 1$ for each sheared data pixel. Then the discrete sensing model in Eq. (21) is changed to a more precise model as

$$g^\ell_{mn} = \sum_r \sum_s \sum_k \sum_u w^\ell_{srmn} t^\ell_{sr} c^\ell_{srk} \beta_{sru} f_{srk}, \quad (32)$$

where the imager is assumed to rotate at a constant speed and the shutter time τ_s is assumed to be constant for each snapshot. Thus, the proportions β_{sru} are unchanged during distinct snapshots. The sensing matrix $\mathbf{H}^\ell$ in Eq. (22) becomes

$$\mathbf{H}^\ell = \mathbf{W}^\ell \mathbf{P}^\ell \mathbf{B}, \quad (33)$$

where the rotation matrix $\mathbf{B}$ contains the proportions β_{sru} for each data pixel. Since each spectral band has the same rotation procedure, $\mathbf{B}$ consists of L diagonal blocks. Each block has the same entries, with the dimensions of $V \times V$. To visualize $\mathbf{H}^\ell$, the test data cube used in displaying Figure 5 and Figure 7 is applied here. Then the corresponding $\mathbf{H}^\ell$ in the continuous rotation model is displayed in Figure 24.

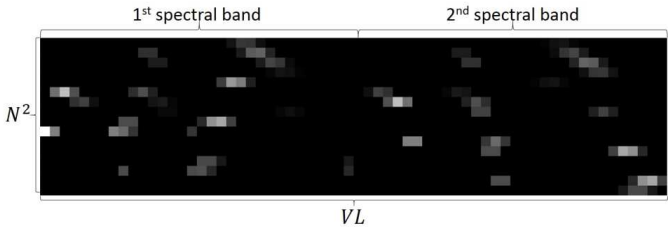

Figure 24. Sensing matrix in the continuous rotation model $\mathbf{H}^\ell$ for a $S_{in} = 8$, $S_{out} = 16$ $R_{in} = 2$, $R_{out} = 1$, $L = 2$ data cube and an $N^2 = 4^2$ FPA.

Denote the rotation period of the imager as τ_r. Assuming K snapshots are desired, the shutter time τ_s should have an upper bound in order to achieve the desired number of snapshots. The acceptable value range of the shutter time is $[0, \tau_r/K]$. Then a normalized shutter time is defined as

$$\eta = \frac{K\tau_s}{\tau_r}, \quad (34)$$

where $\eta \in [0,1]$. In the following experiment, 64-shot measurements are simulated by Eq. (32), applying the continuous rotation model. A comparison between the reconstructions with discrete approximation model and the continuous rotation model is desired. PSNRs are calculated in both reconstructions, as shown in Figure 25.

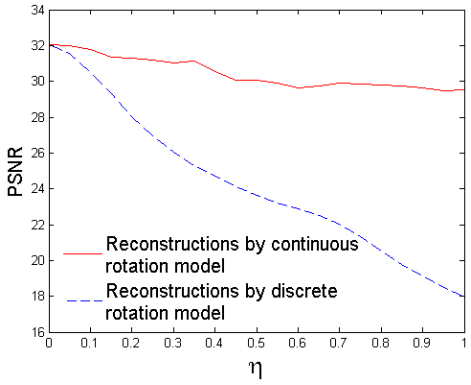

Figure 25. PSNR comparison between discrete rotation model reconstruction and the continuous rotation model reconstruction. 64 continuous rotation compressed projections are simulated with the normalized shutter time η increasing from 0 to 1.

From this experiment, A slight PSNR decrease is observed with the reconstructions by the continuous rotation model when η increases from 0 to 1; while the discrete rotation model suffers from a PSNR decrease with an increasing η. This is because the discrete rotation model fails to model the imager rotation during each FPA integration period, leading to $\mathbf{g} - \mathbf{Hf} \neq \mathbf{0}$. The modelling error increases with larger value of η, reducing reconstruction performance. A further comparison of reconstruction quality between the two approaches is shown in Figure 26, where simulations with $\eta = 0.5$ are performed. The reconstructed image using the discrete rotation model shown in Figure 26 (b) is blurred, with the rotation motion contained. On the other hand, Figure 26 (a) shows a sharp reconstructed image by utilizing the continuous rotation model.

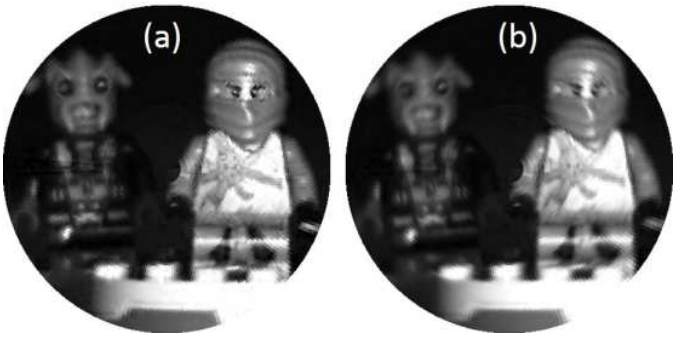

Figure 26. (a) shows the 4th spectral image band reconstructed by applying the continuous rotation model, with 30.1dB PSNR; (b) displays the same spectral band recovered by utilizing the discrete rotation model with the corresponding PSNR 23.6dB.

VI. Conclusion

A compressive spectral imaging system mounted on rotating equipment, such as munitions, has been described. The scene is spatially coded by a polar coded aperture and spectrally modulated by a continuous variable circular bandpass filter. The rotations generate various spatial and spectral modulations. Multiple compressive coded projections are thus captured on the FPA. An inverse algorithm is then applied to reconstruct a spatial spectral data cube. Computer simulations showed accurate spatial and spectral reconstructions when using only a fraction of the full amount of measurements. Design parameters, such as the aperture code geometry and CVF bandwidth, were explored and optimized to enhance image quality. The imager's versatility as a hyper-spectral camera was demonstrated with simulations reconstructing up to 128 spectral bands. A continuous rotation model was developed and simulated, successfully correcting for image blur observed in the discrete model. Although the application in guided munitions requires further research with additional practical considerations, the computational models and the simulation results imply a promising result in the real implementation of the proposed compressive sensing imager.

References

[1] A. Pinker and C. Smith, "Vulnearability of GPS Signal to Jamming", *GPS Solutions*, **3**(2), 1999.

[2] O. Aboutalib, B. Awalt, A. Fung, B. Thai, J. Leibs, T. J. Klausutis, R. Wehling and M. Iames, "All source adaptive fusion for aided navigation in non-GPS environment", *2007 SPIE Defence & Security Symposium, Visual Information Processing XVI*, **6575**, April 2007.

[3] B. Sinopoli, M. Micheli, G. Donato, T. J. Koo, "Vision based navigation for an unmanned aerial vehicle", *Robotics and Automation Proceedings of 2001 ICRA. IEEE International Conference*, **2**, pp.1757-1764, 2001.

[4] R. Sattigeri, A. J. Calise, and J. Evers, "An Adaptive Vision-Based Approach to Decentralized Formation Control", *Journal of Aerospace Computing, Information, and Communication* **1**(12), 502-525, 2004.

[5] A. Cesetti, E. Frontoni, A. Mancini, P. Zingaretti, and S. Longhi, "A vision-based guidance system for UAV navigation and safe landing using natural landmarks", *J. Intell. Robot. Syst.*, **57**, pp. 233257, 2009.

[6] H. Kwon, D. Rosario, N. Gupta, M. Thielke, D. Smith, P. Rauss, P. Gillespie, and N. Nasrabadi, "Hyperspectral Imaging and Obstacle Detection for Robotics Navigation", *U.S. Army Research Laboratory Technical Report* ARL-TR-3639, September 2005.

[7] C. Aguilera, F. Barrera, F. Lumbreras, A.D. Sappa, R. Toledo, "Multispectral image feature points", *Sensors*, **12**(9), pp. 12661-12672, 2012.

[8] Y. Murakami, M. Yamaguchi and N. Ohyama, "Hybrid-resolution multispectral imaging using color filter array," *Opt. Express*, **20**(7), 7173-7183, 2012.

[9] C. Fu, H. Arguello, B. M. Sadler, G. R. Arce, "Compressive Spectral Polarization Imaging By Pixelized Polarizer And Colored Patterned Detector", *J. Opt. Soc. Am. A* **32**, 2178-2188, 2015.

[10] Y. Murakami, M. Yamaguchi and N. Ohyama, "Hybrid-resolution multispectral imaging using color filter array," *Opt. Express*, **20**(7), 7173-7183, 2012.

[11] Y. Garini, I. T. Young, G. McNamara, "Spectral imaging: Principles and applications", *Cytometry Part A*, **69**A(8), 735-747, 2006.

[12] J. H. Apfel, R. F. Illsley, A. J. Thelen, "Circular variable filter", US Patent 3 442 572, 1969.

[13] S. Yang, "Circular, variable, broad-bandpass filters with induced transmission at 200-1100 nm," *Appl. Opt.* **32**, 4836-4842, 1993.

[14] J. M. Lepper, M. K. Diab, "Optical filter for spectroscopic measurement and method of producing the optical filter", US Patent 5 760 910, 1998.

[15] E. M. Anthon, "Compact spectrometer device", US Patent 6 057 925, 2000.

[16] S. P. Morozova, P. A. Morozov, V. I. Sapritsky, B. E. Lisiansky, N. L. Dovgilov, "VNIIOFI Spectroradiometer Based on a Circular Variable Filter for the Spectral Range from 2.5 μm up to 14 μm", *AIP Conf. Proc.* **684**(595), 2003.

[17] M. Dombrowski, J. Lorenz, "Imaging spectroradiometer", US Patent 5 424 543, 1995.

[18] D. Cabib, M. Lavi, A. Gil, E. Ohel, J. Dolev, U. Milman, "A Long Wave Infrared (LWIR) spectral imager (7.7 to 12.3 μ) based on cooled detector array and high resolution Circular Variable Filter (CVF)", *Proc. SPIE 8896, Electro-Optical and Infrared Systems: Technology and Applications X*, **88960R**, 2013.

[19] G. R. Arce, D. J. Brady, L. Carin, H. Arguello, D. S. Kittle, "Compressive coded aperture spectral imaging: An introduction", *Signal Processing Magazine, IEEE*, **31**(1), 105-115, 2014.

[20] M. F. Duarte, M. A. Davenport, D. Takhar, J. N. Laska, T. Sun, K. E. Kelly, and R. G. Baraniuk, "Single-pixel imaging via compressive sampling", *IEEE Signal Processing Magazine* **25**(2), p. 83, 2008.

[21] J. Chen, Y. Wang, and H. Wu, "A coded aperture compressive imaging array and its visual detection and tracking algorithms for surveillance systems", *Sensors*, **12**(11), 14397-14415, 2012.

[22] T. Tsai and D. J. Brady, "Coded aperture snapshot spectral polarization imaging." *Applied optics*, *52*(10), 2153-2161. 2013.

[23] M. E. Gehm, R. John, D. J. Brady, R. M. Willett, and T. J. Schulz, "Single-shot compressive spectral imaging with a dual-disperser architecture", *Optics express*, **15**(21), 14013-14027, 2007.

[24] A. Wagadarikar, R. John, R. Willett, and D. J. Brady, "Single disperser design for coded aperture snapshot spectral imaging", *Applied optics*, **47**(10), B44-B51, 2008.

[25] H. Arguello, H. F. Rueda, and G. R. Arce, "Spatial super-resolution in code aperture spectral imaging", *SPIE Defense, Security, and Sensing, International Society for Optics and Photonics* pp. 83650A-83650A, , 2012.

[26] P. Llull, X. Liao, X. Yuan, J. Yang, D. Kittle, L. Carin, G. Sapiro, and D. J. Brady, "Coded aperture compressive temporal imaging," *Opt. Express 21*, 10526-10545, 2013.

[27] Y. Wu, I. Mirza, G. Arce, and D. Prather, "Demonstration of a DMD-based Compressive Sensing (CS) Spectral Imaging System," *CLEO:2011 - Laser Applications to Photonic Applications, OSA Technical Digest*, 2011.

[28] H. Arguello, and G. R. Arce, "Code aperture agile spectral imaging (CAASI)", *Imaging Systems and Applications, Optical Society of America*, 2011.

[29] H. Arguello, and G. R. Arce. "Code aperture optimization for spectrally agile compressive imaging", *JOSA A* **28**(11), 2400-2413, 2011.

[30] H. Arguello, H. Rueda, Y. Wu, D. W. Prather, G. R. Arce, "Higher-order computational model for coded aperture spectral imaging," *Appl. Opt.* **52**, D12-D21, 2013.

[31] E. J. Candes, M. B. Wakin, "An Introduction To Compressive Sampling", *Signal Processing Magazine, IEEE*, **25**, pp.21-30, 2008.

[32] M. F. Duarte, and R. G. Baraniuk, "Kronecker product matrices for compressive sensing." *2010 IEEE International Conference on Acoustics, Speech and Signal Processing. IEEE*, pp. 3650-3653, 2010.

[33] M. F. Duarte, and R. G. Baraniuk, "Kronecker compressive sensing." *IEEE Transactions on Image Processing* **21**(2), pp.494-504, 2012.

[34] M. Signoretto, R. Van de Plas, B. De Moor, and J. A. Suykens, "Tensor versus matrix completion: a comparison with application to spectral data", *IEEE Signal Processing Letters 18*(7), pp. 403-406, 2011.

[35] M. Golbabaee, and P. Vandergheynst, "Hyperspectral image compressed sensing via low-rank and joint-sparse matrix recovery", *2012 IEEE International Conference On Acoustics, Speech And Signal Processing (ICASSP)*, pp. 2741-2744, 2012.

[36] L. Liu, J. Yan, X. Zheng, H. Peng, D. Guo and X. Qu, "Karhunen-Loève transform for compressive sampling hyperspectral images". *Optical Engineering*, **54**(1), pp. 014106-014106, 2015.

[37] M. Figueiredo, R. D. Nowak, and S. J. Wright, "Gradient projection for sparse reconstruction: Application to compressed sensing and other inverse problems," *IEEE J. of Selected Topics in Signal Processing*, **1**, pp. 586597, 2007.

[38] E. L. Schwartz, D. N. Greve, G. Bonmassar, "Space-variant active vision: Definition, overview and examples", *Neural Networks* **8**, 1297-1308, 1995.

[39] V. J. Traver, A. Bernardino, "A review of log-polar imaging for visual perception in robotics", *Robotics and Autonomous Systems*, **58**(4), 378-398, 2010.

[40] M. H. Buonocore, W. R. Brody, A. Macovsli, and S. L. Wood, "Polar pixel kalman filter for limited data computed tomography (CT) image reconstruction," *SPIE Recent and future developments in medical imaging II*, **26**, pp. 109114, 1979.

[41] T. Herbert, R. Leahy, and M. Singh, "Fast MLE for SPECT using an intermediate polar representation and a stopping criterion," *IEEE Trans. Nucl. Sci.*, **35**, pp. 615619, 1988.

[42] V. Israel-Jost, P. Choquet, S. Salmon, C. Blondet, E. Sonnendrucker, and A. Costantinesco, "Pinhole SPETC imaging: Compact projection/backprojection operator for efficient algebraic reconstruction," *IEEE Trans. Med. Imag.*, **25**, pp. 158167, 2006.

[43] A. C. Sauve, A. O. Hero, W. L. Rogers, S. J. Wilderman, and N. H. Clinthorne, "3D image reconstruction for a Compton SPECT camera model", *IEEE Trans. Nucl. Sci., vol.* **46**, pp. 20752084, 1999.

[44] C. Mora, M. Rafecas, "Polar pixels for high resolution small animal PET", *IEEE Nuclear Science Symposium Conference Record*, **5**, pp.2812-2817, 2006.

Chen Fu received the B.Sc in Electrical Engineering from Nanjing University, Jiangsu China in 2012. He is currently pursuing the Ph.D. degree in Electrical and Computer Engineering at the University of Delaware under the supervision of Dr. Gonzalo R. Arce. His research interests include computational imaging, compressive sensing, optimization and compressive spectral imaging.

Michael L. Don received a bachelors in electrical engineering from Cornell University in 1997. He interned at Digital Equipment Corporation, performing integrated circuit design for their next generation Alpha processor, the fastest processor in the world at that time. After graduating, he worked for Bell Labs where he engaged in the mixed-signal design of read channels for their mass storage group. He then left engineering for a number of years to pursue religious studies. Resuming his career in 2007, he now works for the U.S. Army Research Laboratory specializing in embedded systems, test automation, signal processing, and wireless communication. He is currently pursuing his Ph.D. in electrical engineering at the University of Delaware, researching compressive sensing applications for guided munitions.

Gonzalo R. Arce is the Charles Black Evans Distinguished Professor of Electrical and Computer Engineering at the University of Delaware (UDEL). He holds the J. P. Morgan-Chase Scholar Award and was the 2010-2011 Fulbright-Nokia Distinguished Chair in Information and Communications Technologies. He has served as Department Chair from 2000 to 2009. He was elected member of the Arkansas Academy of Engineering and received the DuPont Young Investigator Award and the NSF Research Initiation Award. He is a Fellow of the Institute of Electrical and Electronic Engineers (IEEE) and a Fellow of the Center for Advanced Studies at the University of Delaware. Dr. Arces research interests include computational imaging, coded aperture optimization, and compressive sensing research and development. He has served as Editor and Guest-Editor of several scientific journal publications of the IEEE, OSA, and SPIE. He holds fifteen US patents and is the author of four books in the areas of imaging and signal processing.